Feature-rich electronic excitations of silicene in external fields

Jhao-Ying Wu,[1,*] Szu-Chao Chen,[2,†] Godfrey Gumbs,[3,‡] and Ming-Fa Lin[2,§]
[1]*Center of General Studies, National Kaohsiung Marine University, Kaohsiung, Taiwan 811*
[2]*Department of Physics, National Cheng Kung University, Tainan, Taiwan 701*
[3]*Department of Physics and Astronomy, Hunter College at the City University of New York, 695 Park Avenue, New York, New York 10065, USA*
(Received 10 January 2016; revised manuscript received 28 October 2016; published 21 November 2016)

We develop a generalized tight-binding model to investigate the Coulomb excitations in monolayer silicene. The atomic interactions, spin-orbit coupling, magnetic and electric fields, as well as the Coulomb interactions are simultaneously included in our calculations. The magnetic field induces interband plasmons with discrete frequency dispersions restricted to quantized energy states. An intraband plasmon, with a higher intensity and continuous dispersion relation, exists in the presence of free carriers. This mode is dramatically transformed into an interband plasma excitation when the magnetic field is increased, leading to abrupt changes in the value of the plasma frequency and its intensity. Specifically, an electric field may separate the spin and valley polarizations and create additional plasmon modes, a unique feature arising from the buckled structure and the existence of noteworthy spin-orbit coupling.

DOI: 10.1103/PhysRevB.94.205427

I. INTRODUCTION

Following the epitaxial synthesis of silicene in 2010 [1–4], a buckled structure in which the silicon atoms are displaced perpendicularly to the basal plane, there have been considerable efforts by researchers to understand its atomic and electronic properties [5–7]. Silicene displays significant spin-orbit coupling (SOC) and electrically tunable electronic properties. A crucial consequence due to an applied electric field ($\vec{E} = E_z\hat{z}$) is that it can open and close the energy band gap, which is a desired functionality for digital electronics applications. It was recently reported that a single silicene layer field-effect transistor has been successfully fabricated and operates at room temperature [8,9]. This moves the material closer to its potential to create more powerful devices. Also, a wealth of fascinating features of silicene have been investigated theoretically, including the quantum spin Hall effect [10,11], the quantum anomalous Hall effect and valley-polarized quantum Hall effect in the presence of an external electric field [12,13], anomalous Hall insulators and single-valley semimetals [14], potential giant magnetoresistance [15], and topologically protected helical edge states [14,16].

The Coulomb excitations, dominated by electron-electron (e-e) interactions, are important for gaining an understanding of the many-particle properties of the carriers in a material. In intrinsic monolayer silicene, low-frequency plasmons hardly exist, mainly because of the vanishing density of states at zero Fermi energy ($E_F = 0$). Such collective modes may be excited by doping or a gate bias to increase the charge carrier-density [17–20], i.e., by raising or lowering the Fermi level to increase the density of states. Alternatively, for an intrinsic sample, free carriers may be generated by increasing the number of thermally excited electrons and holes in the conduction and valence bands, respectively. The intrinsic band gap in silicene is predicted to lead to an interplay between the intraband and interband transitions and create an undamped plasmon at low frequency [21].

A perpendicular magnetic field ($\vec{B} = B_0\hat{z}$) would create cyclotron motion of electrons and form dispersionless Landau levels (LLs), which may largely enhance the low-energy density of states. Unlike graphene, where the $n^{c,v} = 0$ Landau level is pinned at $E_F = 0$, the larger SOC in silicene causes the $n^{c,v} = 0$ level to split into $\pm\lambda_{SOC}/2$ (λ_{SOC} is the strength of SOC) [22,23]. In the presence of an electric field, the single-valley Landau levels are no longer spin degenerate, and the spin-down and spin-up states generate separate energy gaps. The external fields are expected to largely enrich the excitation spectrum.

In this paper we investigate the behavior of magnetoplasmons in silicene in the presence of an applied electric field and a tunable Fermi level taken into account. The calculation is performed with the use of the generalized tight-binding (TB) model that we developed, and which simultaneously incorporates all meaningful interactions, including atomic interaction, spin-orbit coupling, the Coulomb interactions, and the interactions between the charge carriers and the external fields. Since all low-energy states are included, the calculated results are reliable over a wide range of excitation frequencies, field strength, and Fermi energies. The dispersion relation for the magnetoplasmons may be characterized in two categories. One is a propagating mode, while the other is a localized mode. The former is mainly driven by the Coulomb interaction, while the latter is mainly governed by magnetic field effects. The E_z field in the buckled structure induces localized plasmon modes due to the lifting of spin and valley degeneracy. We pay attention to the B_0-dependent plasmon spectrum and observe rich changes in the plasmon features when crossing each critical field strength (B_c). The modulation of the plasmon excitations by the electric and magnetic fields constitutes a possible way to design an active plasmon device in low-buckled materials.

II. METHODS

Similar to graphene, silicene consists of a honeycomb lattice with A and B sublattices. However, silicene has a

*yarst5@gmail.com
†szuchaochen@gmail.com
‡ggumbs@hunter.cuny.edu
§mflin@mail.ncku.edu.tw

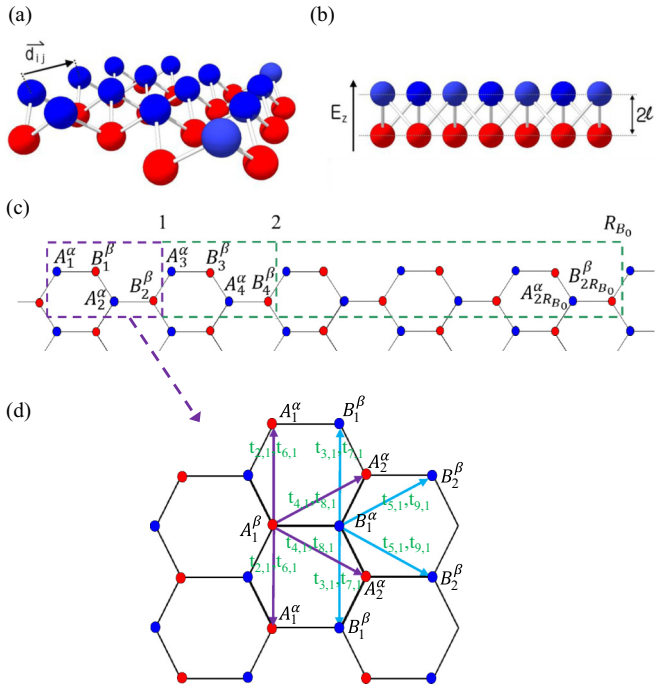

FIG. 1. The lattice geometry of low-buckled silicene in (a) and (b). The two sublattices are separated by a perpendicular distance of $2l$. The staggered sublattice potential energy is produced by an external electric field E_z. The enlarged unit cell in the presence of magnetic field is plotted in (c). The various SOC-related hopping phases are illustrated in (d).

buckled structure, in which the two sublattice planes are separated by a distance of 2ℓ ($\ell = 0.23$ Å), as illustrated in Figs. 1(a) and 1(b). In the TB approximation, the Hamiltonian for silicene in the presence of SOC is given by [12,24]

$$H = -\gamma_0 \sum_{\langle I,J\rangle,\alpha} c^\dagger_{I\alpha} c_{J\alpha} + i\frac{\lambda_{\rm SOC}}{3\sqrt{3}} \sum_{\langle\langle I,J\rangle\rangle,\alpha,\beta} v_{IJ} c^\dagger_{I\alpha} \sigma^z_{\alpha\beta} c_{J\beta} - i\frac{2}{3}\lambda_{R2} \sum_{\langle\langle I,J\rangle\rangle,\alpha,\beta} u_{IJ} c^\dagger_{I\alpha} (\vec{\sigma}\times\hat{d}_{IJ})^z_{\alpha\beta} c_{J\beta} + \ell \sum_{I,\alpha} \mu_I E_z c^\dagger_{I\alpha} c_{I\alpha}. \quad (1)$$

In this notation, $c^\dagger_{I\alpha}$ ($c^\dagger_{J\beta}$) and $c_{I\alpha}$ ($c_{J\beta}$) create and destruct an electronic state with spin polarization α (β) at lattice site I (J), when acting on a chosen wave function. The sums are carried out for nearest-neighbors $\langle I,J\rangle$ or next-nearest-neighbor lattice site pairs $\langle\langle I,J\rangle\rangle$. The first term (I) in Eq. (1) accounts for nearest-neighbor hopping with energy transfer $\gamma_0 = 1.6$ eV. The second term (II) describes the effective SOC for parameter $\lambda_{\rm SOC} = 3.9$ meV, and $\vec{\sigma} = (\sigma_x,\sigma_y,\sigma_z)$ is the vector of Pauli spin matrices. Additionally, we chose $v_{IJ} = \pm 1$ if the next-nearest-neighbor hopping is anticlockwise/clockwise with respect to the positive z axis. In the third term (III), the intrinsic Bychkov-Rashba SOC is included in the next-nearest-neighbor hopping through $\lambda_{R2} = 0.7$ meV, in which $u_{IJ} = \pm 1$ are for the A/B lattice sites, respectively. $\hat{d}_{IJ} = \vec{d}_{IJ}/|d_{IJ}|$ is a unit vector joining two sites I and J on the same sublattice as shown in Fig. 1(a). The staggered sublattice potential energy produced by the external electric field is characterized by the fourth term (IV), where $\mu_I = \pm 1$ for the A/B sublattice sites and $\ell = 0.23$ Å, referring to Fig. 1(b).

Monolayer silicene is assumed to be in a uniform perpendicular magnetic field. The magnetic flux, the product of the field strength, and the hexagonal area is $\Phi = [3\sqrt{3}b^2 B_0/2]/\phi_0$, where ϕ_0 ($= h/e = 4.1\times 10^{-15}$ T m^2) is the magnetic flux quantum and b ($= 2.23$ Å) is the Si-Si bond length. The vector potential $\vec{A} = (B_0 x)\hat{y}$ leads to a new period along the armchair direction, since it can create an extra magnetic Peierls phase, i.e., $\exp\{i[\frac{2\pi}{\phi_0}\int \vec{A}\cdot d\vec{r}]\}$. The unit cell is thus enlarged and its dimension is determined by $R_{B_0} = 1/\Phi$. The reduced first Brillouin zone has an area of $1/(3\sqrt{3}b^2 R_{B_0})$. The enlarged unit cell contains $4R_{B_0}$ Si atoms and the Hamiltonian matrix is a $8R_{B_0}\times 8R_{B_0}$ Hermitian matrix with the spin degree of freedom, as illustrated in Fig. 1(c). Corresponding to $B_0 = 4$ T, where $R_{B_0} = 8000$, the Hamiltonian has a dimension of $64\,000\times 64\,000$. Only the nearest- and next-nearest-neighbor hopping integrals contribute to the nonzero matrix elements. Furthermore, the Landau wave functions are strongly localized at the 1/6, 2/6, 4/6, and 5/6 positions of the enlarged unit cell. The localization centers are determined by the effective momentum due to the magnetic field and the k_y component of the two valleys [25]. As a result, the numerical calculation time related to the Hamiltonian matrix could be largely reduced. The independent Hamiltonian matrix elements are summarized in the Appendix. An illustration of the SOC-related hopping phases are given in Fig. 1(d). Diagonalizing the large Hamiltonian matrix, the eigenenergy $E^{c,v}$ and the wave functions $\Psi^{c,v}$ are obtained, where c and v refer to the conduction and valence bands, respectively.

Whenever a uniform perpendicular magnetic field B_0 is applied to silicene, the electronic states are characterized by dispersionless Landau levels (LLs) whose behavior is governed by the zero-field energy dispersion. The successive LL spacing decreases with increasing energy. Each LL is eightfold degenerate except the $n^{c,v} = 0$ LLs. The eightfold degenerate Landau level is due to the presence of two valleys, two spins, and the relations $\vec{B} = B_0\hat{z}$ and $-B_0\hat{z}$ obtained by considering the complete period of the Peierls phases. The number of nodes from an occupied (unoccupied) LL wave function is equal to the quantum number n^v (n^c). Electrons may be excited from valence LLs to conduction LLs in undoped silicene through electron energy loss spectroscopy (EELS) or when light is absorbed, for example. However, in addition to single-particle excitations between LLs, there are collective magnetoplasmon modes whose frequencies are depolarization shifted due to the Coulomb interaction and are dispersive functions of the momentum transfer q. In our notation, we label each interband inter-LL excitation channel by (n^v, n^c) and the order of the transition by $\Delta n = |n^v - n^c|$. The intraband inter-LL transitions occur in the doped condition and are labeled by (n^c, n^c).

The dispersion relation for the spectrum of collective plasmon modes may be determined from the energy-loss function to be evaluated from the imaginary part of the inverse dielectric function $\mathrm{Im}[-1/\epsilon(q,\omega)]$, where, in the

random-phase approximation (RPA), we have

$$\epsilon(q,\omega) = \epsilon_1(q,\omega) + i\epsilon_2(q,\omega) = \epsilon_0 - v_q \chi^0(q,\omega), \quad (2)$$

with $v_q = 2\pi e^2/q$ being the in-plane Fourier transformation of the bare Coulomb potential energy and $\epsilon_0 = 2.4$ (taken from graphite [26]) is the background dielectric constant due to the deep-energy electronic states. We note that changing ϵ_0 would lead to a vertical shift of the real part of the dielectric function and thus change the peak intensity and position in the energy loss function. However, the plasmon behavior is qualitatively the same. Such a form of dielectric function is utilized in many research studies on two-dimensional (2D) systems, theoretically [27–29] and experimentally [30–32]. The 2D bare response function [26,33–36] is given in Eq. (3). The bra and ket represent the initial and final Landau state wave functions with the respective quantum numbers n and m, where the respective wave vectors are $\vec{k}$ and $\vec{k}+\vec{q}$. In the presence of magnetic field, the system becomes fully quantized. Therefore, the summation becomes a sum over all possible single-particle transitions between bra and ket states. We obtain

$$\chi^0(q,\omega) = \frac{1}{3\sqrt{3}b^2 R_{B_0}} \sum_{n,m} |\langle n;\vec{k}+\vec{q}|e^{i\vec{q}\cdot\vec{r}}|m;\vec{k}\rangle|^2 \times \frac{f(E_n) - f(E_m)}{E_n - E_m - (\omega + i\Gamma)}. \quad (3)$$

The prefactor $1/(3\sqrt{3}b^2 R_{B_0})$ is a normalization constant, meaning that the contribution from each k state in the reduced first Brillouin zone is the same. The equilibrium Fermi-Dirac distribution function is $f(E) = 1/[1+\exp(E-\mu/k_BT)]$, where k_B is Boltzmann constant. Γ is an energy broadening parameter arising from various de-excitation mechanisms, e.g., the optical transitions between the valence- and conduction-band states. μ is the chemical potential whose temperature dependence may be neglected over the range we investigated. The value of the bare response function only relies on the magnitude of the momentum transfer because of the isotropic Landau level spectrum. The energy broadening of the LLs due to the lattice structure is negligible at low temperatures; we set $T = 0$ here.

Details for the calculated results for the Coulomb matrix elements are shown below with

$$|\langle n;\vec{k}+\vec{q}|e^{i\vec{q}\cdot\vec{r}}|m;\vec{k}\rangle = \sum_{s=\alpha,\beta}\sum_{I=1-8R_{B_0}} \langle\phi_z(\vec{r}-\vec{R}_I) \times |e^{-i\vec{q}\cdot(\vec{r}-\vec{R}_I)}|\phi_z(\vec{r}-\vec{R}_I)\rangle [u_{nsI}(\vec{k}+\vec{q})u^*_{msI}(\vec{k})]. \quad (4)$$

Here $\vec{R}_I$ defines the positions of atoms in a unit cell. $u_{msI}(\vec{k})$ $[u_{nsI}(\vec{k}+\vec{q})]$ are the coefficients for the TB wave functions derived from Eq. (1). $\langle\phi_z(\vec{r}-\vec{R}_I)|e^{-i\vec{q}\cdot(\vec{r}-\vec{R}_I)}|\phi_z(\vec{r}-\vec{R}_I)\rangle = C(q) = [1+[\frac{qa_0}{Z}]^2]^{-3}$ was calculated by using hydrogenic wave function [26], where a_0 is the Bohr radius and Z is an effective core charge [37]. We note that the overlapping integrals between neighboring atoms are neglected, an approximation made originally in the 2D model by Blinowski *et al.* [38,39]. For small q, $C(q)$ is very close to 1. The coefficients of the tight-binding functions $u_{msI}(\vec{k})$ are obtained from the diagonalization of the Hamiltonian matrix. They are named as the subenvelope functions, being similar to the Hermite polynomial functions under a magnetic field. Each tight-binding function is a superposition of the product of the amplitudes (coefficients) and the position-dependent $2p_z$ orbital functions (approximated as hydrogenic functions). Since all the π-electronic states are included in our calculations, the strength and frequency of the resonances in $\mathrm{Im}[-1/\epsilon(q,\omega)]$ can be correctly defined. Moreover, the calculations would be reliable in a wide range of the field strength and the chemical potential.

III. RESULTS AND DISCUSSION

A. Landau level spectra

The main difference in the LL spectrum for silicene and graphene is that the former has the $n^c = 0$ and $n^v = 0$ LLs split by the significant SOC. Additionally, the low-lying LL degeneracy and energy are sensitive to a perpendicular electric field, since an on-site potential difference between the A and B sublattices is created. This is revealed in the E_z-dependent LL spectrum shown in Fig. 2(a). From the nodal structure of the wave functions, the quantum number n^c (n^v) for each conduction (valence) LL could be determined from the number of its zeros [40,41]. The quantum number of the dominant sublattice for the highest (lowest) occupied (unoccupied) LL

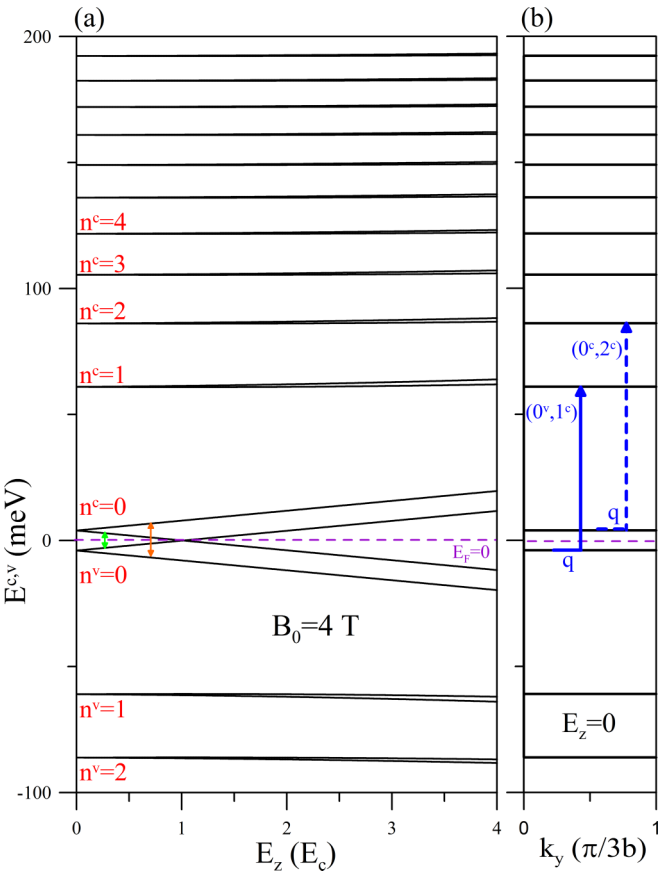

FIG. 2. (a) The Landau level energies as a function of the E-field strength E_z (in unit of $E_c \approx 17$ meV/Å). (b) At $E_z = 0$, the blue solid and dashed lines, respectively, indicate the interband and intraband inter-LL transition channels.

is regarded as the effective quantum number. The highest occupied LL is denoted by n_F, e.g., $n_F = 1$ for two occupied LLs of $n_c = 0$ and 1. Except for the $n^{c,v} = 0$ ones, each LL is eightfold degenerate for every (k_x,k_y) state, and this is attributed to the K and K' valleys, the mirror symmetry of $z = 0$ plane, and the spin degree of freedom. Furthermore, the carrier density for each $n^v \geqslant 1$ LL is $8(\frac{1}{3\sqrt{3}b^2 R_{B_0}})$, where the second factor in this expression is the area of the reduced first Brillouin zone and we refer to Sec. II. The degeneracy of the $n^{c,v} = 0$ LLs is only half that for the others, and the intrinsic band gap determined by the former is about 7.9 meV. A finite E_z field could still split the $n^{c,v} = 0$ LLs. However, the splittings of $n^{c,v} \geqslant 1$ LLs only take place at larger E_z values. This creates two energy gaps with different E_z dependence, as indicated by green and orange arrows in Fig. 2(a). One of these gaps increases with E_z and the other decreases for $E_z < E_c$, a critical electric field. The smaller gap is closed at the critical field $E_c \approx \lambda_{\rm SOC}/\ell = 17$ meV/Å, where the energy difference between the two gaps reaches a maximum. For $E_z > E_c$, both gaps monotonously increase as E_z is increased. The crossing of the $n^{c,v} = 0$ LLs at $E_z = E_c$ is a signature of band inversion associated with the transition from topological insulator to band insulator [42].

Through the Coulomb interactions, electrons may be excited from the valence to conduction LLs for intrinsic silicene for which $n_F = n^v = 0$. A single-particle mode has excitation energy $\hbar\omega_{\rm ex} = E_{n^c}(\vec{k}+\vec{q}) - E_{n^v}(\vec{k})$ by energy and momentum conservation. A pair of numbers $(n^{c,v},n^{c,v})$ is employed to label an inter-LL transition channel. This is illustrated in Fig. 2(b) for two types of transition channels. The pair $(0^v,1^c)$ illustrated by the blue solid arrow denotes an interband inter-LL transition from $n^v = 0$ to $n^c = 1$ LL. It has the same excitation energy as $(1^v,0^c)$ because of the symmetry between the conduction and valence LLs separated by $E_F = 0$ as shown by the purple dashed arrow. As for $(0^c,2^c)$, the blue dashed arrow, it represents the intraband inter-LL transition from $n^c = 0$ to $n^c = 2$ LL. The transition order is denoted as $\Delta n = |n^v - n^c|$, which is useful for categorizing the single-particle excitation (SPE) channels. The number pair is also used to labels a plasmon branch, meaning that the collective excitations are closely related to the SPE channel. This is shown in the plasmon frequency that approaches the SPE energy in the large or small limit of q, as discussed below.

B. Single-particle excitations

The SPE spectrum, determined by the imaginary part ϵ_2 of the dielectric function, is sensitive to changes in E_F and E_z as shown in Figs. 3(a)–3(d). Each peak in ϵ_2 represents a major inter-LL transition channel. The peak intensity is proportional to the Coulomb-matrix elements $|\langle n;\vec{k}+\vec{q}|e^{i\vec{q}\cdot\vec{r}}|m;\vec{k}\rangle|^2$, associated with the wave function overlap between the initial and final states. Based on the characteristics of the Hermite polynomials, a SPE channel with a lower transition order $\Delta n = |n-m|$ has larger Coulomb-matrix elements for a smaller wave vector q. The converse is true for a SPE channel with larger Δn. For example, for intrinsic silicene and small $q = 1$ (in units of 10^5/cm), the three lowest frequency peaks are labeled by $(0^v,1^c)$, $(1^v,2^c)$, and $(2^v,3^c)$ from low to high

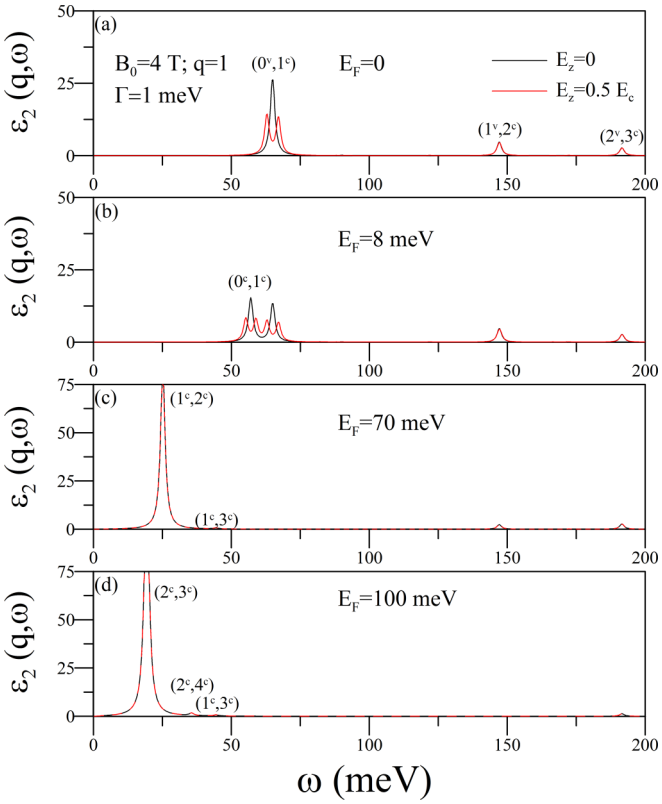

FIG. 3. The imaginary part of the dielectric function $\epsilon(q,\omega)$ for chosen $q = 1$ (in unit of 10^5/cm) and different Fermi energies. The black and red curves correspond to $E_z = 0$ and $E_z = 0.5\ E_c$, respectively.

energy states as illustrated by the black curve in Fig. 3(a). They belong to the interband channels of $\Delta n = 1$.

The channels for SPEs are drastically altered under extrinsic condition, as we have shown for various Fermi energies in Fig. 3. If the $n^c = 0$ LL is occupied with $n_F = n^c = 0$ and $E_F = 8$ meV in Fig. 3(b), the intensity of the $(0^v,1^c)$ interband excitation is reduced by a factor of 2 as half the spectral weight is shifted to a lower-energy intraband peak for the $(0^c,1^c)$ mode. The two channels $(0^c,1^c)$ and $(0^v,1^c)$ are Pauli blocked when E_F crosses the $n^c = 1$ LL for $n_F = 1$ and $E_F = 70$ meV in Fig. 3(c). The replacement is a more prominent and lower-frequency peak due to the intraband channel $(1^c,2^c)$. The significant changes in peak intensity and frequency arise from the in-phase inter-LL transition and the reduced LL spacing at higher energy. This is even more evident for a larger n_F, e.g., $n_F = 2$ and $E_F = 100$ meV in Fig. 3(d).

A finite E_z generates spin- and valley-polarized LLs [Fig. 2(a)] and enriches the SPE spectra. At $E_F = 0$, peak $(0^v,1^c)$ is split into two according to different valley transitions for a single spin [red curve in Fig. 3(a)]. The two interband peaks respectively exhibit the red and blue shifts when E_z is increased from zero to E_c, and their frequency difference reaches a maximum as the lower band gap completely closes at $E_z = E_c$. But for $E_z > E_c$, both split peaks move to higher frequencies due to the reopening of the lower gap (not shown). If both $n^c = 0$ LLs are occupied [Fig. 3(b)], there exist four robust spin- and valley-polarized peaks. They result

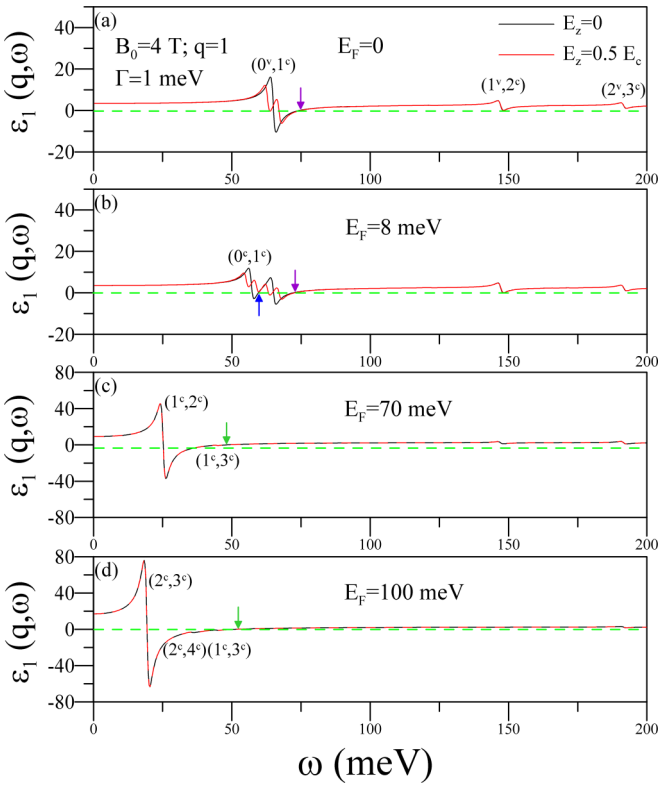

FIG. 4. The real part of the dielectric functions $\epsilon(q,\omega)$ for the same conditions of Fig. 3. The black and red curves correspond to $E_z = 0$ and $E_z = 0.5\ E_c$, respectively.

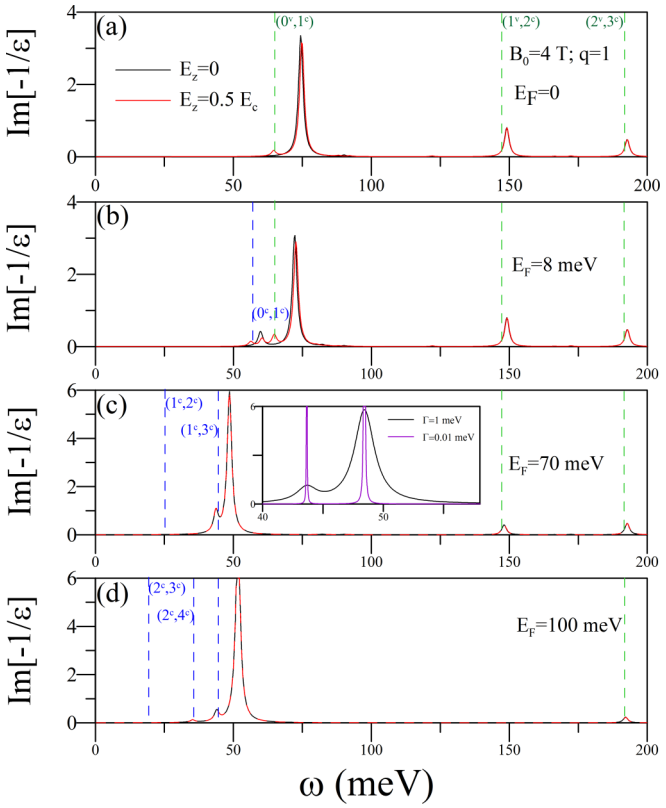

FIG. 5. The energy-loss functions for $q = 1$ and different Fermi energies. The vertical blue (green) dashed lines indicate the intraband (interband) SPE energies. Also shown in the inset of (c) is a comparison between two values for the broadening parameter Γ.

from two-spin and two-valley transitions. This phenomenon is absent at $n_F \geqslant 1$ [Figs. 3(c) and 3(d)], because with more occupied conduction LLs, the transitions from and to the $n^{c,v} = 0$ LLs own a larger Δn and are faint at a small q.

C. Real part of the dielectric function

The real part ϵ_1 of the dielectric function is related to its imaginary part ϵ_2 through the Kramers-Kronig relations and our results are presented in Figs. 4(a) through 4(d). A pair of asymmetric peaks in ϵ_1 correspond to a symmetric peak in ϵ_2, and ϵ_1 could vanish at some frequencies. If a zero point for ϵ_1 occurs where ϵ_2 is small, then this corresponds to weak damping of a plasmon mode. For example, there are zeros for ϵ_1 between the $(0^v,1^c)$ and $(1^v,2^c)$ peaks, indicated by purple arrows in Figs. 4(a) and 4(b). At these zeros, there is not much Landau damping by the SPEs. On the other hand, the intraband peak $(0^c,1^c)$ presents a zero point denoted by a blue arrow in Fig. 4(b), at a finite ϵ_2 that comes from the adjacent interband channel $(0^v,1^c)$. This $\epsilon_1 = 0$ leads to a strongly damped plasmon. Specifically, for $n_F \geqslant 1$, the intraband channels collectively contribute to one zero point, as illustrated by the green arrows in Figs. 4(c) and 4(d). This means that at a very high E_F, all low-frequency transition states make contributions to one solution of $\epsilon_1 = 0$, as for a classical zero-B_0 condition [43].

D. The loss function

The energy-loss function, defined as $\mathrm{Im}[-1/\epsilon(q,\omega)]$, is useful for understanding the collective excitation spectra measured by either inelastic light scattering [44–46] or EELS [31,32,47–49]. Each spectral peak in $\mathrm{Im}[-1/\epsilon(q,\omega)]$ may be interpreted as corresponding to the excitation of a plasmon mode having different degrees of Landau damping. For example, the most intense interband plasmon mode is located between the SPE energies for $(0^v,1^c)$ and $(1^v,2^c)$ as shown by the green vertical dashed lines in Fig. 5(a). This peak corresponds to a $\epsilon_1 = 0$ solution and small ϵ_2 [purple arrow in Fig. 4(a)]. However, the second and third peaks, which are close to the SPE energies of $(1^v,2^c)$ and $(2^v,3^c)$, respectively, are relatively weak due to considerable Landau damping.

The characteristics of the intensity and frequency of plasmon modes change noticeably as E_F crosses a specific LL. The spectral weight of the lowest-frequency interband plasmon $(0^v,1^c)$ is partially transferred to a lower-frequency intraband mode $(0^c,1^c)$ when the $n^c = 0$ LL is occupied and which is shown as the black curve in Fig. 5(b). The latter has significant Landau damping and is weaker than the former. More free conduction electrons produce an enhanced intraband plasmon, as illustrated in Fig. 5(c) for $n_F = 1$. The intraband peak grows in intensity obviously with the increment of n_F, e.g., $n_F = 2$ in Fig. 5(d). This is due to the increased (decreased) number of intraband (interband) channels plotted in the blue (green) vertical dashed lines. Changing the broadening parameter Γ

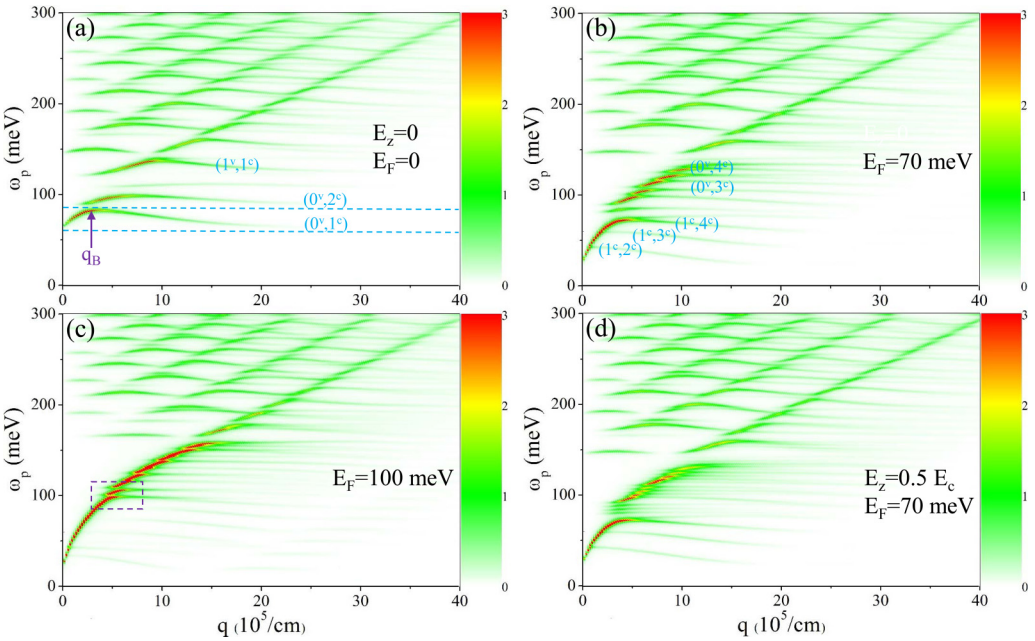

FIG. 6. The q-dependent plasmon spectrum at $E_z = 0$ for (a) $E_F = 0$, (b) $E_F = 70$ meV, and (c) $E_F = 100$ meV. That at $E_z = 0.5\ E_c$ and $E_F = 70$ meV is plotted in (d) for comparison. The color scale represents the intensity of the energy-loss function.

does not alter the magnetoplasmon frequencies, but it does affect the spectral widths and intensities. The smaller the chosen value for Γ, the narrower spectral width and the stronger intensities are obtained, as illustrated in the inset of Fig. 5(c). A quite strong plasmon peak indicates that this mode is due to the collective excitations of all free carriers in the conduction LLs.

An electric field provides a tool for a tuning the dispersion relation of the collective excitations. It creates new peaks and reduces the threshold frequency due to the separated spin and valley polarizations corresponding to the red curves in Figs. 5(a) and 5(b). The extra plasmon modes experience rather strong Landau damping, since the splitting energies between any two LLs are small compared to other LL spacings. However, the splitting energies may be increased by making E_z larger, which results in higher weights of the newly created peaks (not shown here). We note that with $n_F \geqslant 1$ [see Figs. 5(c) and 5(d)], the E_z-field effects will be evident only for larger wave vector q, as demonstrated below.

E. The magnetoplasmon excitations

The magnetoplasmon spectrum possesses an intriguing q dependence. Intrinsic silicene possesses interband plasmon modes which are strongly confined to lie between two neighboring SPE channels in a limited q range. For example, the lowest-frequency plasmon branch $(0^v,1^c)$ lies between the SPE energies of $(0^v,1^c)$ and $(0^v,2^c)$, as illustrated by the two horizontal blue-dashed lines in Fig. 6(a). This plasmon is strongly damped in both the short and long wavelength limits, with its frequency close to the SPE energy of $(0^v,1^c)$. All the q-dependent magnetoplasmon frequencies possess humplike features, indicating that charge oscillations behave quite differently below and above a critical momentum indicated by a purple arrow. In our notation, q_B corresponds to zero group velocity and is determined by comparable characteristic lengths in the charge oscillations and cyclotron motion. If $q < q_B$, the group velocity is positive and the plasmon intensity grows with increasing momentum. However, the opposite is true for $q > q_B$. The value of q_B is increased by stronger B_0. For a plasmon-excitation channel, the larger the transition order $\triangle n$, a higher rate of increase in q_B as a function of B_0 is obtained [27]. The peculiar dependence of q_B on B_0 may result in a rich B_0-dependent plasmon spectrum, as demonstrated in Figs. 7 through 9.

The properties of intraband magnetoplasmons are in sharp contrast with those arising from interband transitions in (q,ω) space. For $n_F = 1$ and $E_F = 70$ meV, we show in Fig. 6(b) that the lowest-frequency interband plasmon branch $(0^v,1^c)$ no longer exists and is replaced by a combination of three intraband modes, i.e., $(1^c,2^c)$, $(1^c,3^c)$, and $(1^c,4^c)$. The three intraband modes form a continuous branch which exhibits a longer range of positive group velocity and higher intensity. Additionally, the disappearance of the interband plasmon $(1^v,1^c)$, marked in Fig. 6(a), helps to enhance the other interband modes, such as $(0^v,3^c)$ and $(0^v,4^c)$. Although these interband plasmons are close to each other, they disperse independently because they experience a strong transverse restoring force coming from the magnetic field. With larger $n_F = 2$ when $E_F = 100$ meV in Fig. 6(c), the intraband magnetoplasmon has a more obvious continuous branch, due to the increased number of intraband channels. The gap between the intraband plasmon and the lowest-frequency interband mode is reduced, as shown by the purple rectangle. An electric field induces additional discrete subbranches mainly as a result of the LL splitting, as shown in Fig. 6(d) for $E_F = 70$ meV and $E_z = 0.5\ E_c$. The newly created modes in the range of $75 \leqslant \omega \leqslant 100$ meV are weakly dispersive due to the combined effects of the buckled structure and magnetic field. Their momentum range, frequency, and number can be

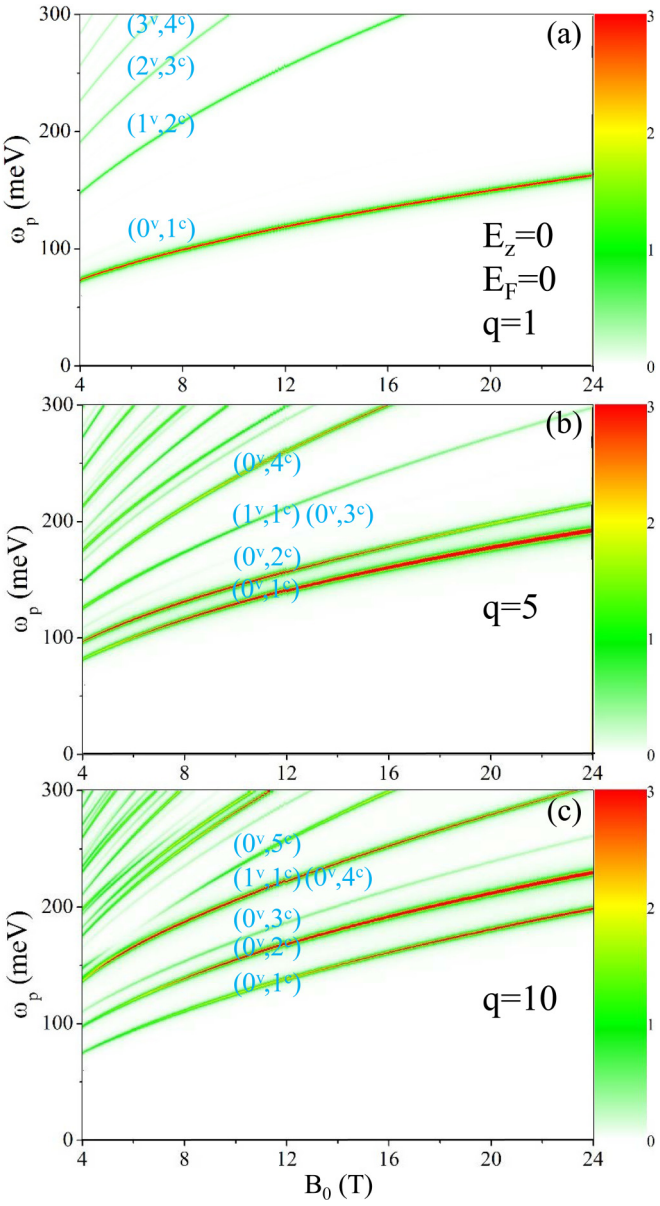

FIG. 7. The B_0-dependent plasmon spectrum for $E_F = 0$ for various chosen q in (a)–(c).

easily modulated by varying E_z and E_F. These subbranches, coming from the spin- and valley-polarized LLs, may play an important role in fine-tuning details of the magnetoplasmon spectrum.

The intensity and frequency of plasmon modes exhibit unusual B_0 dependence for various momentum transfer values and Fermi energies. The interband plasmon frequencies for intrinsic silicene, shown in Fig. 7, increase monotonically with B_0 due to the enlarged LL spacings. Specially, the plasmon intensities are drastically changed as B_0 is increased, depending on LL degeneracy, momentum transfer, and q_B. At long wavelength [$q \simeq 1$ in Fig. 7(a)], the interband plasmons are dominated by the SPE channels with $\Delta n = 1$, determined by the characteristics of Hermite polynomial functions. Their intensities are enhanced by B_0, since there are more states in each LL. When q is increased and becomes comparable with the q_B for the $(0^v,2^c)$ mode [$q = 5$ in Fig. 7(b)], $\Delta n = 1$ and 2 (purple arrow) plasmon branches can exist simultaneously, and their intensities are strengthened and weakened by the increase of B_0, respectively. The different B_0 dependence mainly comes from the competition between q and q_B. The latter is augmented on account of the enlarged ratio of carrier oscillation wavelength to magnetic length. For $\Delta n = 1$, magnetoplasmon modes with $q = 5 > q_B$, an increasing B_0 causes q_B to move closer to q, enhancing the collective oscillations, e.g., the $(0^v,1^c)$ mode. However, the opposite holds true for the $(0^v,2^c)$ mode with $q = 5 < q_B$. This means that the increasing B_0 will cause the value of q to deviate from q_B and weaken the plasmon intensity. The above-mentioned plasmons can be enhanced simultaneously when q is larger than q_B of all modes, e.g., $q = 10$ in Fig. 7(c).

The plasmon spectrum for $n_F = 1$ experiences an abrupt change in intensity, frequency, and bandwidth at a critical field, e.g., $B_c \simeq 5.5$ T for $E_F = 70$ meV; see Figs. 8(a) through 8(c). Above B_c, all free conduction electrons are accommodated in the $n^c = 0$ LL, so that the threshold plasmon mode is dramatically changed from the intraband $(1^c,2^c)$ to the interband $(0^v,1^c)$ at small q in Fig. 8(a). In contrast, the other interband channels pass the critical field continuously. This unusual behavior for the intraband and interband modes is a feature which distinguishes them. As q is increased in Fig. 8(b), obvious changes in the plasmon spectrum after crossing B_c include the discontinuous transformation from the lowest-frequency intraband mode $(1^c,4^c)$ to the interband one $(0^v,1^c)$ and the newly created interband branch $(1^v,1^c)$. For large q in Fig. 8(c), there are more modes involving the $n^c = 1$ LL, like $(1^c,5^c)$ and $(1^c,8^c)$. These modes disappear at $B_0 > B_c$ and thus create more discontinuities in the plasmon spectrum. Apparently, the momentum transfer is a critical factor for tuning the B_0-dependent plasmon spectrum.

Starting with $n_F = 2$, there are two critical B_c fields for which n_F may be decreased to $n_F - 1$, as shown in Figs. 9(a) through 9(c). For $E_F = 100$ meV, the first critical magnetic field occurs at $B_{c1} \simeq 5.5$ T (the same as in Fig. 8), and the second one is at $B_{c2} \simeq 10.8$ T. For small momentum in Fig. 9(a), the lowest-frequency plasmon mode is intraband $(2^c,3^c)$ before B_{c1} is achieved, while between B_{c1} and B_{c2} is $(1^c,2^c)$. Beyond B_{c2}, the threshold mode is replaced by the interband excitation $(0^v,1^c)$. The redistributions of strong plasmon modes are obtained for various values of q, referring to Figs. 9(b) and 9(c). In general, the plasmon spectra are different in the three B_0-field ranges defined by $0 < B_0 < B_{c1}$, $B_{c1} < B_0 < B_{c2}$, and $B_{c2} < B_0$. These clearly reflect the characteristic features of $n_F = 2$, $n_F = 1$, and $n_F = 0$. The discontinuous structure in the plasmon spectrum at $B_c's$ should be verified by EELS reflection [31,32,47,48] and reflection [49] as well as inelastic light scattering [44–46]. The magnetically tunable plasmon spectrum, with strong dependence on the momentum transfer as well as the intraband and interband modes, may be useful for the design of magnetoplasmonic components for various applications.

The physical reasons of the qualitative difference between the intraband and interband plasmons are summarized below. The inter-LL magnetoelectronic excitations come to exist when electrons are excited from the occupied LLs to the

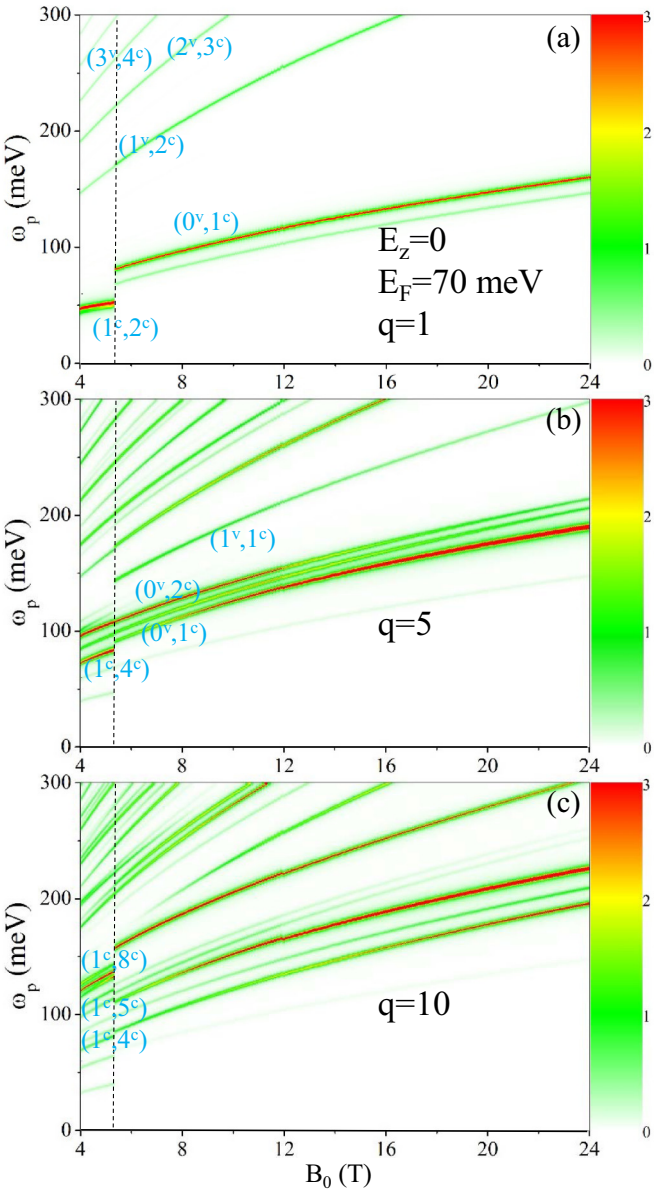

FIG. 8. Same plot as Fig. 7, except that $E_F = 70$ meV.

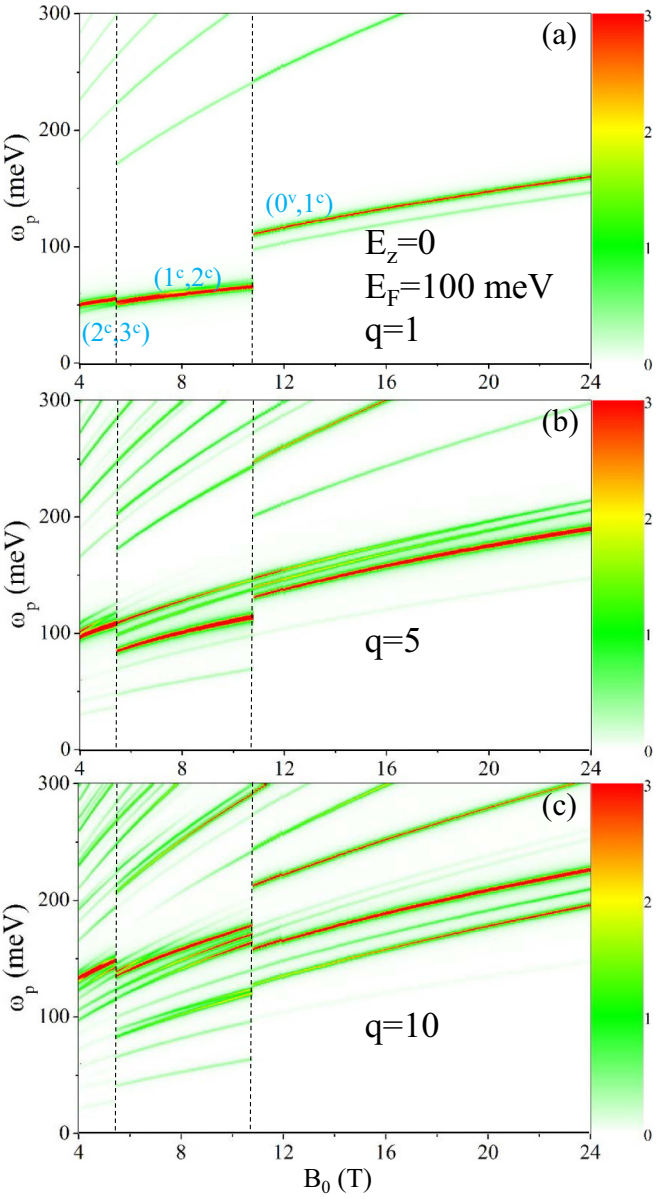

FIG. 9. Same plot as Fig. 7, but for $E_F = 100$ meV.

unoccupied ones. They could be further categorized into the intraband (c to c) and the interband (v to c) inter-LL transitions. The important differences between them include the intensity, energy and number of SPEs, and plasmon modes. The former have stronger SPE spectra [Figs. 4(c) and 4(d)], since the Coulomb matrix elements [Eq. (4)] are due to linearly symmetric superposition of the tight-binding functions of two different sublattices. However, the weaker spectra in the latter come from linearly antisymmetric superposition. The first few intraband SPE channels present the close frequencies so that they could induce collective excitations together. This intraband plasmon, which arises from all free carriers in conduction band, exhibits a continuous dispersion relation [Figs. 6(b) and 6(c)]. Its strong intensity will be suppressed by the interband SPEs at large q's. There exist several interband plasmons corresponding to interband inter-LL transitions. Such modes possess weaker intensities because of the serious Landau damping of the higher-energy inter-LL transitions.

The definition and further explanation on the propagating mode and a localized mode are presented. Plasmons are quanta of the electron density oscillations. The derivative of frequency versus momentum represents the group velocity of oscillation wave. A strong dispersion relation in intraband plasmon [Figs. 6(b) and 6(c)] clearly indicates that the collective excitations behave as a propagating wave with a continuous wavelength of $2\pi/q$. Compared with the magnetic field, the e-e interactions dominate the main features of intraband plasmons. On the other hand, there are strongly competitive relations between the transverse magnetic quantization and the longitudinal Coulomb interactions in interband plasmons. Such plasmons exhibit very weak dispersion relations, being strongly confined between two SPE frequencies [Fig. 6(a)]. They have rather small group velocity; therefore they could be categorized

as the localized modes. From a classical point of view, the localized modes show that the charge density oscillations experience a strong restoring force arising from the magnetic field.

IV. SUMMARY AND CONCLUSIONS

A generalized TB model has been developed to investigate the Coulomb excitations of monolayer silicene. The atomic interactions, spin-orbit coupling, magnetic and electric field effects, as well as the electron-electron interactions are simultaneously taken into account. The excitation spectrum is efficiently solved by using an exact diagonalization method. This makes our procedure very suitable to deal with the quantized electronic excitations. The calculated results are reliable over a wide range of excitation frequencies, field strength, and chemical potential. The presented methodology may be extended to other 2D materials. It may become a tool in the search for better nanoplasmonic materials and attract further research in this area.

Monolayer silicene, with the buckled structure and significant SOC, exhibits unique electronic excitations. The special relation between the Coulomb interactions and the external electric and magnetic fields determines the characteristics of the excitation spectra. There are two types of low-frequency plasmons, namely the interband and intraband ones. They could coexist at low doping. The important differences between them are clearly exhibited in the (q,ω) plots. The interband plasmons have discrete peaks in the energy-loss function for which their frequencies are confined by the magnetically quantized energy states. Their frequency dispersion relations are marked by a critical momentum q_B. The group velocity is positive and negative for $q < q_B$ and $q > q_B$, respectively, a consequence of the competition between the transverse cyclotron force and the longitudinal Coulomb interaction. The intraband plasmon involves multiple intraband transition channels which collectively contribute to a strong peak in the loss spectrum. Such a mode appears as a continuous branch in the (q,ω)-phase diagram with positive group velocity, which is strongly driven by the Coulomb interaction. Moreover, the B_0-dependent plasmon spectra are mainly determined by the wavelength of charge carrier oscillations, the magnetic length, and the LL degeneracy. As the B_0 field is increased, the intraband plasmon is considerably transformed into an interband mode, as indicated by an abrupt change of the spectral width, frequency, and intensity. An electric field can make independent spin and valley polarizations and induce more localized plasmon modes. In other words, a combination of spin valleytronics and magnetoplasmonics may be fulfilled in monolayer silicene.

ACKNOWLEDGMENT

This work was supported by the MOST 105-2112-M-022-001.

APPENDIX

Only the fourth interaction in Eq. (1) is a diagonal matrix independent of the Peierls phase. Through detailed calculations, the independent Hamiltonian matrix elements, associated with the additional position-dependent Peierls phases, are given in Eqs. (A1)–(A9) which now follow. That is,

$$\text{(I)}\quad \langle B_J^\alpha | H | A_I^\beta \rangle = \gamma_0 \sum_{\langle I,J\rangle} \frac{1}{N} \exp\left[i\vec{k}\cdot\left(\vec{R}_{A_I^\beta} - \vec{R}_{B_J^\alpha}\right)\right] \exp\left\{ i\left[\frac{2\pi}{\phi_0}\int_{\vec{R}_{A_I^\beta}}^{\vec{R}_{B_J^\alpha}} \vec{A}\cdot d\vec{r}\right]\right\} = \gamma_0 t_{1,I}\delta_{I,J+1}\delta_{\alpha,\beta} + \gamma_0 s\delta_{I,J}\delta_{\alpha,\beta}, \quad \text{(A1)}$$

where $\vec{R}_{A_I^\beta}$ and $\vec{R}_{B_J^\alpha}$ denote lattice sites for the A and B sublattices, respectively, with spin polarizations β and α. Also, "I" indicates the starting sublattice site. For the kinetic energy, the nearest-neighbor matrix element includes the phase-related term of $t_{1,I} = \exp\{i[-k_x\frac{b}{2} - k_y\frac{\sqrt{3}b}{2} + \pi\frac{\Phi}{\phi_0}(I-1+\frac{1}{6})]\} + \exp\{i[-k_x\frac{b}{2} + k_y\frac{\sqrt{3}b}{2} - \pi\frac{\Phi}{\phi_0}(I-1+\frac{1}{6})]\}$ and a specific term of $s = \exp[i(-k_x b)]$. The vector potential can generate more complicated hopping phases in the SOC-related interactions, as presented in Eqs. (A2)– (A9). For example, $t_{2,1}$ ($t_{8,1}$) denotes the phase term for next-nearest-neighbor hopping from A_1^β to A_1^α (A_1^β to A_2^α), corresponding to the effective SOC (intrinsic Rashba SOC). An illustration of the SOC-related hopping phases are given in Fig. 1(d). Next,

$$\text{(II)}\quad \langle A_J^\alpha | H | A_I^\beta \rangle = \frac{\lambda_{\rm SOC}}{3\sqrt{3}} \sum_{\langle\langle I,J\rangle\rangle} \frac{1}{N} \exp\left[i\vec{k}\cdot\left(\vec{R}_{A_I^\beta} - \vec{R}_{A_J^\alpha}\right)\right] \exp\left\{ i\left[\frac{2\pi}{\phi_0}\int_{\vec{R}_{A_I^\beta}}^{\vec{R}_{A_J^\alpha}} \vec{A}\cdot d\vec{r}\right]\right\} + E_z\ell = \frac{\lambda_{\rm SOC}}{3\sqrt{3}} t_{2,I}\delta_{I,J}\delta_{\alpha,\beta} + E_z\ell, \quad \text{(A2)}$$

where $t_{2,I} = \exp i[k_y a + 2\pi\frac{\Phi}{\phi_0}(I-1)] - \exp i[-k_y a - 2\pi\frac{\Phi}{\phi_0}(I-1)]$. Also,

$$\langle B_J^\alpha | H | B_I^\beta \rangle = \frac{\lambda_{\rm SOC}}{3\sqrt{3}} \sum_{\langle\langle I,J\rangle\rangle} \frac{1}{N} \exp\left[i\vec{k}\cdot\left(\vec{R}_{B_I^\beta} - \vec{R}_{B_J^\alpha}\right)\right] \exp\left\{ i\left[\frac{2\pi}{\phi_0}\int_{\vec{R}_{B_I^\beta}}^{\vec{R}_{B_J^\alpha}} \vec{A}\cdot d\vec{r}\right]\right\} - E_z\ell = \frac{\lambda_{\rm SOC}}{3\sqrt{3}} t_{3,I}\delta_{I,J}\delta_{\alpha,\beta} - E_z\ell, \quad \text{(A3)}$$

where $t_{3,I} = \exp i\{-k_y a - 2\pi\frac{\Phi}{\phi_0}[(I-1)+\frac{1}{3}]\} - \exp i\{k_y a + 2\pi\frac{\Phi}{\phi_0}[(I-1)+\frac{1}{3}]\}$.

$$\left\langle A_J^\alpha \middle| H \middle| A_I^\beta \right\rangle = \frac{\lambda_{\rm SOC}}{3\sqrt{3}} \sum_{\langle\langle I,J\rangle\rangle} \frac{1}{N} \exp\left[i\vec{k}\cdot\left(\vec{R}_{A_I^\beta} - \vec{R}_{A_J^\alpha}\right)\right] \exp\left\{i\left[\frac{2\pi}{\phi_0}\int_{\vec{R}_{A_I^\beta}}^{\vec{R}_{A_J^\alpha}} \vec{A}\cdot d\vec{r}\right]\right\} = \frac{\lambda_{\rm SOC}}{3\sqrt{3}} t_{4,I}\delta_{I,J-1}\delta_{\alpha,\beta}, \tag{A4}$$

where $t_{4,I} = \exp i\{k_x\frac{3}{2}b - k_y\frac{a}{2} - \pi\frac{\Phi}{\phi_0}[(I-1)+\frac{1}{2}]\} - \exp i\{k_x\frac{3}{2}b + k_y\frac{a}{2} + \pi\frac{\Phi}{\phi_0}[(I-1)+\frac{1}{2}]\}$. Additionally,

$$\left\langle B_J^\alpha \middle| H \middle| B_I^\beta \right\rangle = \frac{\lambda_{\rm SOC}}{3\sqrt{3}} \sum_{\langle\langle I,J\rangle\rangle} \frac{1}{N} \exp\left[i\vec{k}\cdot\left(\vec{R}_{B_I^\beta} - \vec{R}_{B_J^\alpha}\right)\right] \exp\left\{i\left[\frac{2\pi}{\phi_0}\int_{\vec{R}_{B_I^\beta}}^{\vec{R}_{B_J^\alpha}} \vec{A}\cdot d\vec{r}\right]\right\} = \frac{\lambda_{\rm SOC}}{3\sqrt{3}} t_{5,I}\delta_{I,J-1}\delta_{\alpha,\beta}, \tag{A5}$$

where $t_{5,I} = \exp i\{k_x\frac{3}{2}b - k_y\frac{a}{2} - \pi\frac{\Phi}{\phi_0}[(I-1)+\frac{5}{6}]\} - \exp i\{k_x\frac{3}{2}b + k_y\frac{a}{2} + \pi\frac{\Phi}{\phi_0}[(I-1)+\frac{5}{6}]\}$.

$$\text{(III)}\quad \left\langle A_J^\alpha \middle| H \middle| A_I^\beta \right\rangle_{\alpha\neq\beta} = \frac{2}{3}\lambda_{R2} \sum_{\langle\langle I,J\rangle\rangle} \frac{1}{N} \exp\left[i\vec{k}\cdot\left(\vec{R}_{A_I^\beta} - \vec{R}_{A_J^\alpha}\right)\right] \exp\left\{i\left[\frac{2\pi}{\phi_0}\int_{\vec{R}_{A_I^\beta}}^{\vec{R}_{A_J^\alpha}} \vec{A}\cdot d\vec{r}\right]\right\} = \frac{2}{3}\lambda_{R2} t_{6,I}\delta_{I,J}, \tag{A6}$$

where $t_{6,I} = \exp i[k_y a + 2\pi\frac{\Phi}{\phi_0}(I-1) - \frac{\pi}{2}] + \exp i[-k_y a - 2\pi\frac{\Phi}{\phi_0}(I-1) + \frac{\pi}{2}]$. We also introduce

$$\left\langle B_J^\alpha \middle| H \middle| B_I^\beta \right\rangle_{\alpha\neq\beta} = \frac{2}{3}\lambda_{R2} \sum_{\langle\langle I,J\rangle\rangle} \frac{1}{N} \exp\left[i\vec{k}\cdot\left(\vec{R}_{B_I^\beta} - \vec{R}_{B_J^\alpha}\right)\right] \exp\left\{i\left[\frac{2\pi}{\phi_0}\int_{\vec{R}_{B_I^\beta}}^{\vec{R}_{B_J^\alpha}} \vec{A}\cdot d\vec{r}\right]\right\} = \frac{2}{3}\lambda_{R2} t_{7,I}\delta_{I,J}, \tag{A7}$$

where $t_{7,I} = \exp i\{k_y a + 2\pi\frac{\Phi}{\phi_0}[(I-1)+\frac{1}{3}] - \frac{\pi}{2}\} + \exp i\{-k_y a - 2\pi\frac{\Phi}{\phi_0}[(I-1)+\frac{1}{3}] + \frac{\pi}{2}\}$.

$$\left\langle A_J^\alpha \middle| H \middle| A_I^\beta \right\rangle_{\alpha\neq\beta} = \frac{2}{3}\lambda_{R2} \sum_{\langle\langle I,J\rangle\rangle} \frac{1}{N} \exp\left[i\vec{k}\cdot\left(\vec{R}_{A_I^\beta} - \vec{R}_{A_J^\alpha}\right)\right] \exp\left\{i\left[\frac{2\pi}{\phi_0}\int_{\vec{R}_{A_I^\beta}}^{\vec{R}_{A_J^\alpha}} \vec{A}\cdot d\vec{r}\right]\right\} = \frac{2}{3}\lambda_{R2} t_{8,I}\delta_{I,J-1}, \tag{A8}$$

where $t_{8,I} = \exp i\{k_x\frac{3}{2}b + k_y\frac{a}{2} + \pi\frac{\Phi}{\phi_0}[(I-1)+\frac{1}{2}] - \frac{\pi}{6}\} + \exp i\{k_x\frac{3}{2}b - k_y\frac{a}{2} - \pi\frac{\Phi}{\phi_0}[(I-1)+\frac{1}{2}] + \frac{\pi}{6}\}$. Finally, we have

$$\left\langle B_J^\alpha \middle| H \middle| B_I^\beta \right\rangle_{\alpha\neq\beta} = \frac{2}{3}\lambda_{R2} \sum_{\langle\langle I,J\rangle\rangle} \frac{1}{N} \exp\left[i\vec{k}\cdot\left(\vec{R}_{B_I^\beta} - \vec{R}_{B_J^\alpha}\right)\right] \exp\left\{i\left[\frac{2\pi}{\phi_0}\int_{\vec{R}_{B_I^\beta}}^{\vec{R}_{B_J^\alpha}} \vec{A}\cdot d\vec{r}\right]\right\} = \frac{2}{3}\lambda_{R2} t_{9,I}\delta_{I,J-1}, \tag{A9}$$

where $t_{9,I} = \exp i\{k_x\frac{3}{2}b + k_y\frac{a}{2} + \pi\frac{\Phi}{\phi_0}[(I-1)+\frac{5}{6}] - \frac{\pi}{6}\} + \exp i\{k_x\frac{3}{2}b - k_y\frac{a}{2} - \pi\frac{\Phi}{\phi_0}[(I-1)+\frac{5}{6}] + \frac{\pi}{6}\}$.

[1] B. Aufray, A. Kara, S. Vizzini, H. Oughaddou, C. Léandri, B. Ealet, and G. Le Lay, Appl. Phys. Lett. **96**, 183102 (2010).

[2] P. Vogt, P. De Padova, C. Quaresima, J. Avila, E. Frantzeskakis, M. C. Asensio, A. Resta, B. Ealet, and G. Le Lay, Phys. Rev. Lett. **108**, 155501 (2012).

[3] L. Chen, C.-C. Liu, B. Feng, X. He, P. Cheng, Z. Ding, S. Meng, Y. Yao, and K. Wu, Phys. Rev. Lett. **109**, 056804 (2012).

[4] Z. L. Liu, M. X. Wang, J. P. Xu, J. F. Ge, G. L. Lay, P. Vogt, D. Qian, C. L. Gao, C. Liu, and J. F. Jia, New J. Phys. **16**, 075006 (2014).

[5] N. Takagi, C. L. Lin, K. Kawahara, E. Minamitani, N. Tsukahara, M. Kawai, and R. Arafune, Prog. Surf. Sci. **90**, 1 (2015).

[6] H. Oughaddou, H. Enriquez, M. R. Tchalala, H. Yildirim, A. J. Mayne, A. Bendounan, G. Dujardin, M. A. Ali, and A. Kara, Surf. Sci. **90**, 46 (2015).

[7] S. Balendhran, S. Walia, H. Nili, S. Sriram, and M. Bhaskaran, Small **11**, 640 (2015).

[8] L. Tao, E. Cinquanta, D. Chiappe, C. Grazianetti, M. Fanciulli, M. Dubey, A. Molle, and D. Akinwande, Nat. Nanotech. **10**, 227 (2015).

[9] L. L. Guy, Nat. Nanotech. **10**, 202 (2015).

[10] C.-C. Liu, W. Feng, and Y. Yao, Phys. Rev. Lett. **107**, 076802 (2011).

[11] M. Tahir and U. Schwingenschlögl, Sci. Rep. **3**, 1075 (2013).

[12] M. Ezawa, Phys. Rev. Lett. **109**, 055502 (2012).

[13] H. Pan, Z. Li, C. C. Liu, G. Zhu, Z. Qiao, and Y. Yao, Phys. Rev. Lett. **112**, 106802 (2014).

[14] M. Ezawa, Phys. Rev. B **87**, 155415 (2013).

[15] S. Rachel and M. Ezawa, Phys. Rev. B **89**, 195303 (2014).

[16] H. R. Chang, J. Zhou, H. Zhang, and Y. Yao, Phys. Rev. B **89**, 201411 (2014).

[17] F. Schedin, A. K. Geim, S. V. Morozov, E. W. Hill, P. Blake, M. I. Katsnelson, and K. S. Novoselov, Nat. Mater. **6**, 652 (2007).

[18] P. Willke, J. A. Amani, A. S. Thakur, T. Kotzott, T. Druga, S. Weikert, K. Maiti, H. Hofsass, and M. Wenderoth, Nano Lett. **15**, 5110 (2015).

[19] L. A. Ponomarenko, B. D. Belle, R. Jalil, L. Britnell, R. V. Gorbachev, A. K. Geim, K. S. Novoselov, A. H. Castro Neto, L. Eaves, and M. I. Katsnelson, J. Appl. Phys. **113**, 136502 (2013).

[20] C. Baeumer, D. Saldana-Greco, J. M. P. Martirez, A. M. Rappe, M. Shim, and L. W. Martin, Nat. Commun. **6**, 6136 (2015).

[21] J. Y. Wu, S. C. Chen, and M. F. Lin, New J. Phys. **16**, 125002 (2014).
[22] C. J. Tabert and E. J. Nicol, Phys. Rev. B **88**, 085434 (2013).
[23] K. H. Shakouri, P. Vasilopoulos, V. Vargiamidis, and F. M. Peeters, Phys. Rev. B **90**, 235423 (2014).
[24] C. C. Liu, H. Jiang, and Y. Yao, Phys. Rev. B **84**, 195430 (2011).
[25] Y. K. Huang, S. C. Chen, Y. H. Ho, C. Y. Lin, and M. F. Lin, Sci. Rep. **4**, 7509 (2014)
[26] K. W.-K. Shung, Phys. Rev. B **34**, 979 (1986).
[27] J. Y. Wu, S. C. Chen, O. Roslyak, G. Gumbs, and M. F. Lin, ACS Nano **5**, 1026 (2011).
[28] S. Yuan, R. Roldan, and M. I. Katsnelson, Phys. Rev. B **84**, 035439 (2011).
[29] M. Pisarra, A. Sindona, P. Riccardi, V. M. Silkin, and J. M. Pitarke, New J. Phys. **16**, 083003 (2014).
[30] S. Y. Shin, C. G. Hwang, S. J. Sung, N. D. Kim, H. S. Kim, and J. W. Chung, Phys. Rev. B **83**, 161403(R) (2011).
[31] T. Eberlein, U. Bangert, R. R. Nair, R. Jones, M. Gass, A. L. Bleloch, K. S. Novoselov, A. Geim, and P. R. Briddon, Phys. Rev. B **77**, 233406 (2008).
[32] C. Kramberger, R. Hambach, C. Giorgetti, M. H. Rummeli, M. Knupfer, J. Fink, B. Buchner, L. Reining, E. Einarsson, S. Maruyama, F. Sottile, K. Hannewald, V. Olevano, A. G. Marinopoulos, and T. Pichler, Phys. Rev. Lett. **100**, 196803 (2008).
[33] H. Ehrenreich and M. H. Cohen, Phys. Rev. **115**, 786 (1959).
[34] K. W. Chiu and J. J. Quinn, Phys. Rev. B **9**, 4724 (1974).
[35] R. Roldán, J.-N. Fuchs, and M. O. Goerbig, Phys. Rev. B **80**, 085408 (2009).
[36] O. L. Berman, G. Gumbs, and Y. E. Lozovik, Phys. Rev. B **78**, 085401 (2008).
[37] C. Zener, Phys. Rev. **36**, 51 (1930).
[38] J. Blinowski, N. H. Hau, C. Rigaux, J. P. Vieren, R. le Toullee, G. Furdin, A. Herold, and J. Melin, J. Phys. (Paris) **41**, 47 (1980)
[39] J. Blinowski and C. Rigaux, J. Phys. (Paris) **41**, 667 (1980)
[40] Y. H. Lai, J. H. Ho, C. P. Chang, and M. F. Lin, Phys. Rev. B **77**, 085426 (2008).
[41] C. Y. Lin, J. Y. Wu, Y. C. Ou, Y. H. Chiu, and M. F. Lin, Phys. Chem. Chem. Phys. **17**, 26008 (2015).
[42] M. Ezawa, New J. Phys. **14**, 033003 (2012).
[43] T. Ando, A. B. Fowler, and F. Stern, Rev. Mod. Phys. **54**, 437 (1982).
[44] D. Richards, Phys. Rev. B **61**, 7517 (2000).
[45] T. Devereaux and R. Hackl, Rev. Mod. Phys. **79**, 175 (2007).
[46] A. F. García-Flores, H. Terashita, E. Granado, and Y. Kopelevich, Phys. Rev. B **79**, 113105 (2009).
[47] P. Wachsmuth, R. Hambach, M. K. Kinyanjui, M. Guzzo, G. Benner, and U. Kaiser, Phys. Rev. B **88**, 075433 (2013).
[48] C. T. Pan, R. R. Nair, U. Bangert, Q. Ramasse, R. Jalil, R. Zan, C. R. Seabourne, and A. J. Scott, Phys. Rev. B **85**, 045440 (2012).
[49] T. Langer, H. Pfnur, H. W. Schumacher, and C. Tegenkamp, Appl. Phys. Lett. **94**, 112106 (2009).